

**Starshade Technology Development Activity  
Milestone 1B:**

**Demonstration of High Contrast in  
Broadband Light at a Flight-like Fresnel Number**

Anthony Harness, N. Jeremy Kasdin, Michael Galvin

Princeton University

Stuart Shaklan, Kunjithapatham Balasubramanian, Victor White, Karl  
Yee, Richard Muller, Philip Dumont, Simon Vuong, Phillip Willems

Jet Propulsion Laboratory, California Institute of Technology

March 28, 2019

# Contents

<b>Executive Summary</b>	<b>1</b>
<b>1 Introduction</b>	<b>2</b>
<b>2 Experiment Update</b>	<b>2</b>
2.1 Testbed upgrades . . . . .	3
2.2 Broadband starshade mask . . . . .	3
2.3 Data collection procedures . . . . .	4
<b>3 Experiment Data</b>	<b>4</b>
<b>4 Model Comparison</b>	<b>5</b>
<b>5 Milestone Analysis</b>	<b>8</b>
<b>6 Discussion</b>	<b>12</b>
6.1 Comparing M1A and M1B results . . . . .	12
6.2 Model accuracy . . . . .	12
6.3 Mitigating the thick screen effects . . . . .	13
<b>7 Conclusion</b>	<b>14</b>
<b>References</b>	<b>15</b>
<b>Appendix A: Rayleigh Scattering Model</b>	<b>16</b>
<b>Appendix B: Scalar Model Validation using M1A Mask at 725 nm</b>	<b>20</b>

# Executive Summary

We report the results of high-contrast measurements with a laboratory starshade mask at four laser wavelengths spanning 640 - 725 nm. Using the same experimental configuration reported in Milestone 1A, with the starshade set up in a flight-like diffraction regime with the Fresnel number  $N = 12.2$  at the inner working angle (IWA) for the longest wavelength, we find that on average 15% of the IWA has a contrast better than  $10^{-10}$ , the average contrast at the IWA is  $2.0 \times 10^{-10}$ , 75% of the search space is below  $10^{-10}$ , and the minimum observed contrast in the open regions of the mask is  $2 \times 10^{-11}$ . At a slightly larger radius where  $N = 15$ , 48% of the contrast is better than  $10^{-10}$  and the average contrast is  $1.3 \times 10^{-10}$ .

As reported in M1A, the performance is limited by the interaction of light with the edges of the gold-coated silicon mask, which acts as a thick screen. As shown through finite-difference time-domain (FDTD) modeling, the mask openings effectively narrow by  $\sim 250$  nm, attenuating the light and introducing a small phase shift. Experimental results are in good agreement with the models.

In addition to the high contrast measurements, we have measured the M1A mask at a wavelength slightly outside its designed suppression band and verify the accuracy of the scalar model at a contrast of  $10^{-8}$ .

We have also improved the model of Rayleigh scattering in the testbed and show that  $\sim$  half of the observed suppression, and almost all of the wide-angle contrast, is caused by Rayleigh scattering by air molecules. The contrast floor from Rayleigh scattering is  $\sim 10^{-11}$ .

The high contrast measurements, while limited by the thick screen effects, are nonetheless at a level entirely consistent with high-efficiency detection of exo-earths in the habitable zones of their stars. Furthermore, scaling arguments from our vector diffraction models suggest that the performance impact of thick screen effects will be greatly reduced with increasing spatial scale of the starshade.

Finally, we discuss the predicted outcome of repeating the experiments in a larger facility so that the thick screen propagation effects would be reduced and the expected contrast level at the IWA would be well below  $10^{-10}$ .

# 1 Introduction

The Exoplanet Exploration Program (ExEP) has chartered the Starshade Technology Activity, called S5, to develop starshade technology to Technology Readiness Level (TRL) 5 for a future space mission. S5 is focused on optical, mechanical, and formation flying technologies culminating in a series of milestones to be completed between 2019 and 2023.<sup>1</sup> The first three milestones focus on the demonstration of optical performance at flight-required levels.

Milestone 1A demonstrated  $10^{-10}$  contrast at the IWA of a small-scale starshade mask in monochromatic light and verified we can design a starshade capable of producing scientifically useful contrast levels.<sup>2</sup> The continuation of this milestone using broadband light increases the applicability of the experiment to a more flight-like configuration and demonstrates that the previous results hold across a bandpass of greater scientific interest. Here we report on the second of the optical performance milestones:

**Milestone 1B:** Small-scale starshade mask in the Princeton Testbed demonstrates  $1 \times 10^{-10}$  instrument contrast at the inner working angle at multiple wavelengths spanning  $\geq 10\%$  bandpass and Fresnel number  $\leq 15$  at the longest wavelength.

This report details the experiment and results supporting the completion of Milestone 1B and serves as an addendum to the previous Milestone 1A Report. Herein we refer to the recently completed Milestone 1A effort simply as M1A and the current effort as M1B. We describe updates to the experiment since M1A, present the broadband experimental data with comparison to results from our vector diffraction model, and provide a quantitative measure of the regions around the starshade that meet the milestone. In Appendix A, we present results from a Rayleigh scattering model that explains the contrast floor as due to scattering from air molecules. Appendix B compares contrast measurements of the M1A mask to the slightly larger M1B mask at a wavelength where the contrasts differ by more than an order of magnitude. We find the measurements to be in excellent agreement with diffraction models.

Across the 85 nm bandpass, contrast  $< 10^{-10}$  is observed over 15% of the IWA, while the average contrast at the IWA is  $2.0 \times 10^{-10}$  with a floor of  $2 \times 10^{-11}$ . At a slightly larger radius with Fresnel Number  $N = 15$  at the longest wavelength, 48% of the contrast is below  $10^{-10}$  and the average contrast is  $1.3 \times 10^{-10}$ .

## 2 Experiment Update

The experiment for this milestone is very similar to that of M1A, but conducted at four discrete wavelengths spanning  $\sim 85$  nm. The specific wavelengths were chosen to span the widest bandpass possible with our starshade design and to be evenly distributed across the bandpass. The four wavelength channels and the values of various wavelength-dependent parameters are presented in Table 1. The spectral line width of each laser channel is  $< 2$  nm.

Laser Channel	Peak Wavelength	ND Filters	Measured ND Attenuation	Fresnel Number	Free Space Correction
1	641 nm	OD7	$8.19 \times 10^{-8}$	13.83	1.03
2	660 nm	OD7	$1.98 \times 10^{-7}$	13.43	0.944
3	699 nm	OD8+OD1	$1.28 \times 10^{-7}$	12.68	1.05
4	725 nm	OD8+OD1	$7.40 \times 10^{-7}$	12.23	1.05

Table 1: Wavelengths of the multi-channel laser. Also provided are the neutral density (ND) filters and their attenuation factor. The Fresnel numbers are provided for a starshade of radius 12.53 mm and effective distance of 17.72 m. The effective distance and free space calibration correction are summarized in the M1A Report.

## 2.1 Testbed upgrades

The laser, fiber, and spatial filter are the same as those in M1A, but now all four channels of the multi-channel laser are utilized. The channels are switched by manually changing the fiber connection at the laser, outside of the testbed. The only major hardware update to the testbed was to move the neutral density filter to immediately in front of the camera aperture. In M1A, the ND filter was placed between the collimating lens and the spatial filter in the laser station. Inserting the ND filter for calibration observations caused slight movement of the spatial filter focus in the pinhole, which changed the transmission through the pinhole. This change in transmission was consistent and well characterized before observations. However, the pinhole transmission is no longer consistent when changing the fiber between laser channels, so the ND filter was moved downstream to the front of the camera. If the pinhole transmission is changed between laser channels, it will be the same for both the science and calibration observations and cancels out in the contrast definition.

We also changed the motorized ND filter changer to a larger version that holds four filters. The ND filter from M1A was found to be inadequately gray with attenuation decreasing with wavelength. To maintain a constant source brightness for all channels, a separate filter is required for channels 3 and 4. The ND filter values are summarized in Table 1.

## 2.2 Broadband starshade mask

The starshade mask used for M1A was designed to work over a narrow (10 nm) bandpass centered at 638 nm. In the optimization routine used to solve for the apodization function, we minimized the maximum allowed petal curvature to help loosen manufacturing tolerances, which naturally caused the bandpass to be wider than required. The bandpass for this mask (Figure 1) was wide enough for our broadband measurements, but did not overlap with wavelengths available with our laser, so we shifted the bandpass to be centered around 680 nm by scaling the size of the starshade by  $\sqrt{680/638}$ . This is possible due to scalar diffraction being identical for a given Fresnel number. The bandpass of this new mask (Figure 1) is now centered nicely across our laser channels. The radius of this mask (at the peak apodization value) is 12.53 mm and we provide the Fresnel number at each wavelength in Table 1.

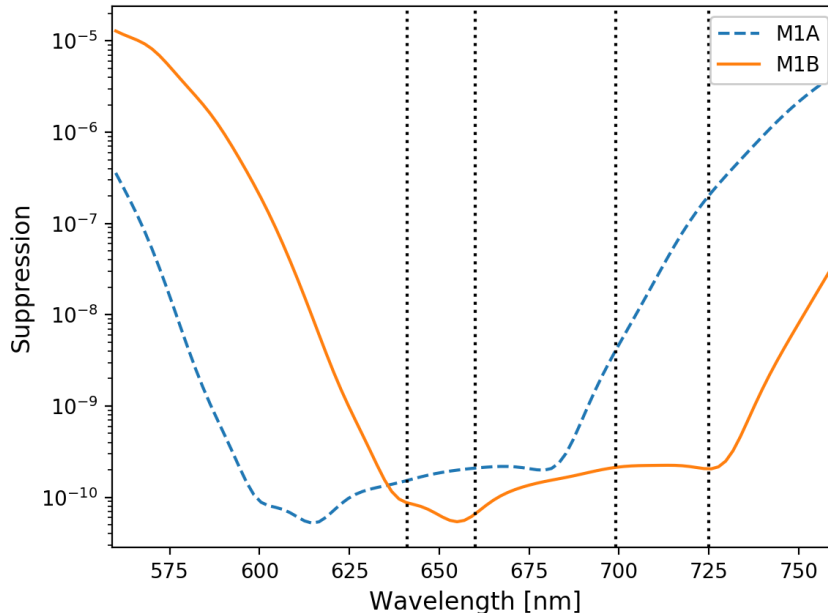


Figure 1: Suppression as a function of wavelength for the starshade designs used in the different experiments. The vertical lines mark the wavelengths of the four laser channels. In the lab configuration, a suppression of  $10^{-10}$  results in a contrast at the IWA of  $\sim 10^{-12}$ .

The manufacturing process for the mask used in this experiment was the same as that in M1A with the exception being the thickness of the SOI device layer. In M1A, the mask (with manufacturing iteration number DW17) had a device layer thickness of  $\sim 2 \mu m$ ; for M1B, the mask (DW21) has a device layer thickness of  $\sim 3 \mu m$ . The additional thickness was discovered at the end of the manufacturing process; the silicon-on-insulator (SoI) thickness of the DW21 wafer was out of specification from a batch of wafers marked with SoI thickness  $2.0 \pm 0.7 \mu m$ .

### 2.3 Data collection procedures

The data collection for an individual wavelength channel is identical to that summarized in Appendix B of the M1A Report. After all data for one channel is collected, the fiber is changed to a new channel (without opening the testbed) and the process is repeated. The camera was originally focused for 641 nm light and is not refocused between testing the different channels.

## 3 Experiment Data

We conducted a full observation run for each wavelength channel, the results of which are summarized in Table 2. Note that the output power of each laser channel is different and results require normalization by calibration observations. Figure 2 shows contrast maps for

all 4 observation runs. The polarization lobes are again visible in the same orientation as with the M1A mask and aligned with the measured state of polarization. The lobes for the Channel 2 run are not symmetric about the mask, which we attribute to either the telescope not being perfectly centered in the shadow or to a non-uniform illumination of the mask. The peak contrast of the M1B data is slightly higher than that of M1A (see Figure 19 of the M1A Report), which is consistent with a thicker mask; the contrast scales linearly with the mask thickness.

Wavelength Channel	Date	Science Exposure Time	Science Peak Counts	Calibration Exposure Time	Calibration Peak Counts
1	2/25/2019	1200 s	46000	10 s	36500
2	2/26/2019	800 s	55119	2.5 s	42000
3	2/27/2019	1200 s	25000	10 s	42000
4	2/28/2019	1800 s	38000	2.5 s	45000

Table 2: Summary of contrast observations for each wavelength channel.

## 4 Model Comparison

As in the M1A Report, we provide only a qualitative comparison of the experimental results with simulated results generated from a scalar + vector diffraction model in order to attribute the contrast limitation to non-scalar effects. There is good qualitative agreement between model and experiment, but further improvement and sophistication of the model would be needed to bring the two into a full, quantitative agreement.

Figures 3 and 4 show the reduction in amplitude and the change in phase as a function of width between petals ( $w$ ) for the four wavelengths; results are calculated from an FDTD solution of Maxwell’s equation<sup>3</sup> through a  $2\ \mu\text{m}$  thick silicon mask which is acting as a thick screen. The amplitude and phase results for a  $3\ \mu\text{m}$  thick mask are  $\sim 1.2$  times larger but have the same form as the  $2\ \mu\text{m}$  mask, as shown in Harness *et al.*<sup>4</sup>

The amplitude decreases as  $w^{-1}$ , meaning the total light reduction at a given radius is constant across the petal and is localized to the edge of the mask. The amount of energy lost is dependent on the material properties and thickness of the mask; for our mask, the loss of energy is equivalent to the petals being under-etched by  $\sim 125\ \text{nm}$ . The change in phase decreases more quickly with width (and is close to zero for p-polarization), which suggests a more complex, waveguiding interaction between opposing petals. The amplitude and phase dependence on wavelength is very small, consistent with the constant peak contrast across the bandpass seen in the experimental data.

Figures 6 – 9 show experimental and model comparisons for the four wavelength channels. In order to match the experimental data, the results from the FDTD simulation had to be scaled by  $\sim 50\%$ , effectively reducing the thickness of the mask. This discrepancy may be due to the real mask having a tapered and/or scalloped edge, as shown in Figure 5; we believe that a detailed measurement of the mask edge and simulation of that profile will bring the two into closer agreement.

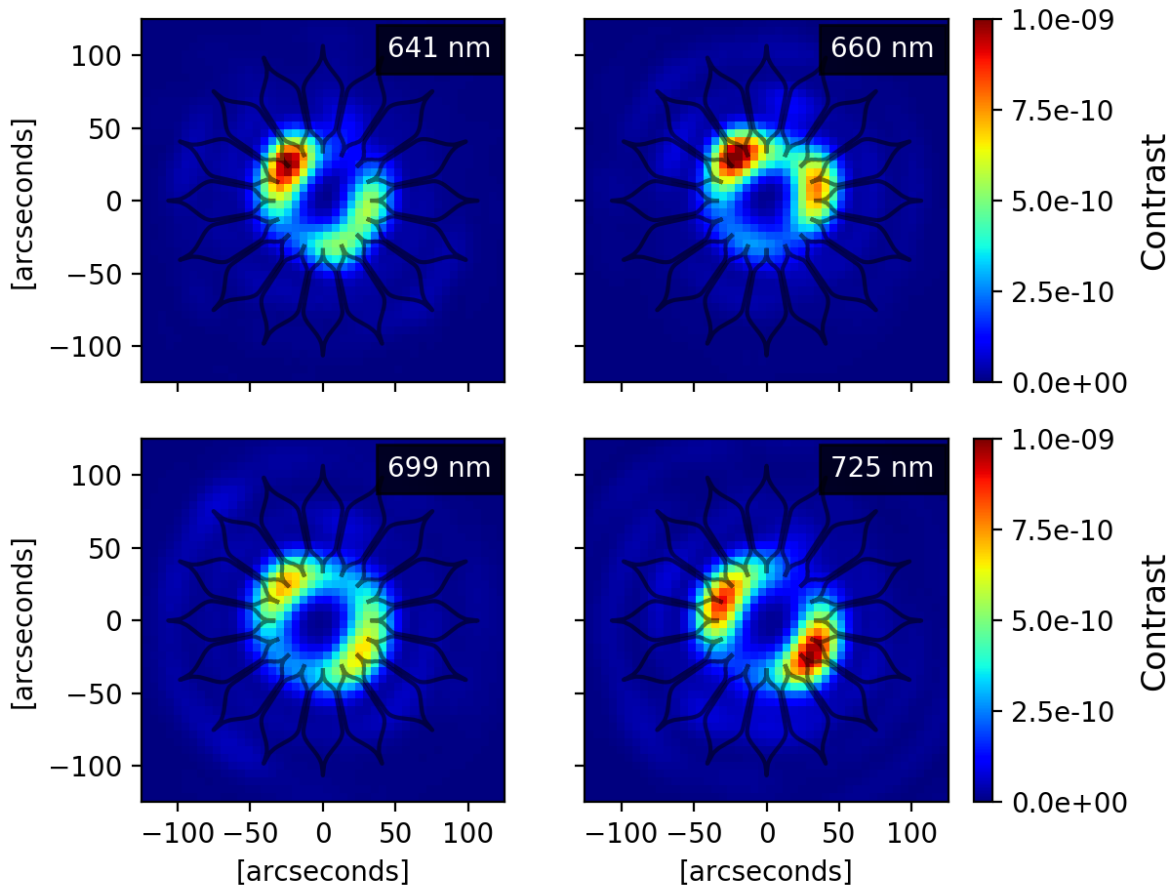


Figure 2: Contrast maps for the four wavelength channels.

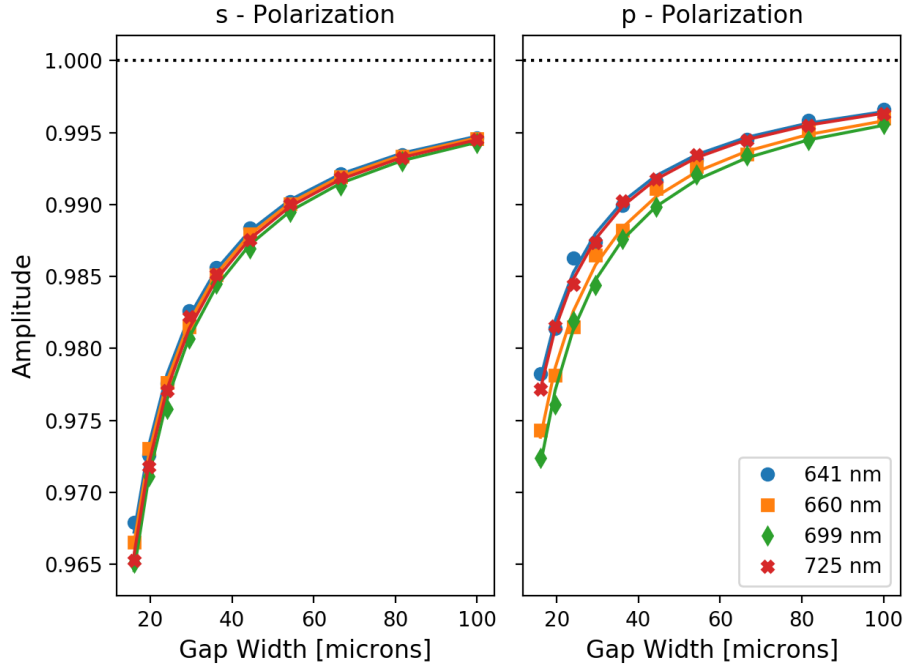


Figure 3: Results from FDTD simulation of a  $2 \mu m$  thick mask showing the reduction in amplitude as a function of width between petals. Solid lines are fits to the data of the form  $1 - \gamma/w$ , where  $\gamma$  is a wavelength- and polarization-dependent constant.

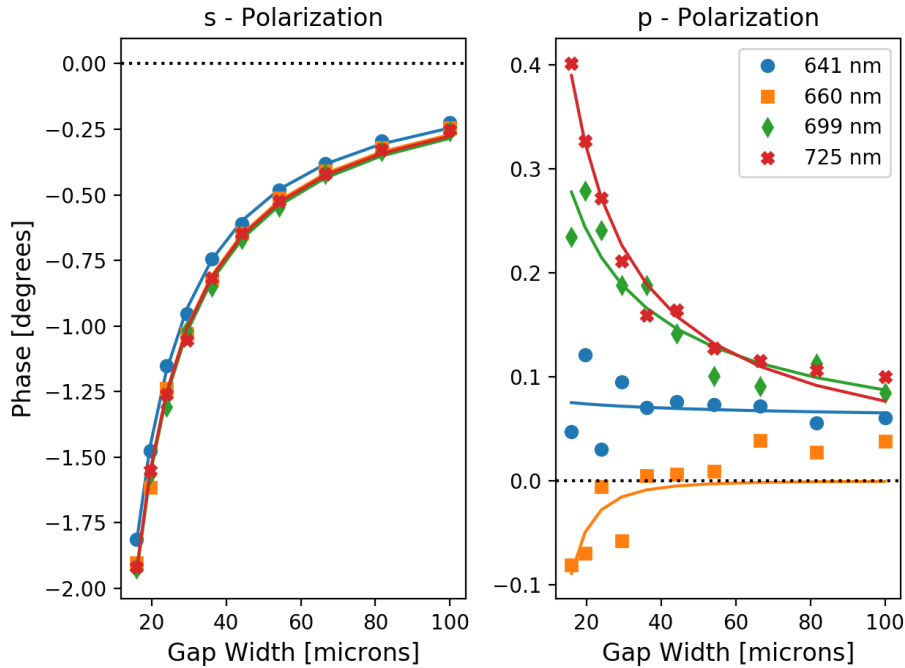


Figure 4: Results from FDTD simulation of a  $2 \mu m$  thick mask showing the change in phase as a function of width between petals. Solid lines are fits to the data of the form  $\gamma/w^\alpha$ , where  $\gamma, \alpha$  are wavelength- and polarization-dependent constants.

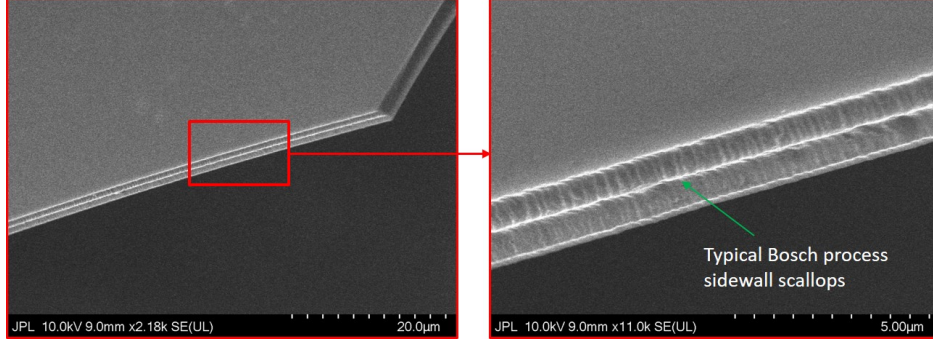


Figure 5: Scanning electron microscope image of a starshade mask. The mask imaged here was  $2\ \mu\text{m}$  thick and was not viable for high-contrast measurement due to several small manufacturing defects.

The dominant effect of non-scalar diffraction is localized to a small region at the edge of the mask, whose size is determined by the material properties and thickness of the edge. The optical edge of the flight-scale starshade will be made of different materials than that of the lab mask, but will not have a significantly thicker edge, so we can expect the edge region to be comparable in size. However, the petals will be  $1000\times$  larger than in the lab. We believe this will dominate over any thick screen effects and the non-scalar diffraction will be negligible. Further analysis of light propagation past the material and geometry of the edges of the flight starshade is needed before this assessment can be made definitively.

## 5 Milestone Analysis

Our milestone is to achieve  $10^{-10}$  contrast at the inner working angle of the starshade across a broad bandpass. Table 3 presents the fraction of the IWA for which we achieve this contrast at each wavelength. It shows that we meet this milestone over a modest portion of the IWA annulus for the first two wavelength channels and do not meet the milestone for most of the longer wavelength channels. In addition to reporting the results at the IWA, where the apodization function reaches its peak value, we report the results at the radius at which the Fresnel number equals 15 at the longest wavelength, consistent with the definition in the milestone. Also presented in Table 3 is the fraction of the total search space that has contrast better than  $10^{-10}$ . The search space is defined as the annulus between the IWA and the OWA (outer working angle; where the apodization drops below its peak value as the apodization of the outer ring begins). Refer to Section 7 of the M1A Report for further details on the procedure for deriving these results.

Figure 10 shows the aperture contrast for the four runs with a mask applied to those pixels that exceed  $10^{-10} - 3\sigma$ . The weighted moving average of the fraction of pixels that meet the milestone contrast at each radius is presented in Figure 11. Due to broadening of the PSF, the fraction is lower for the longer wavelength channels. The fraction is anomalously high for channel 2, due to the uneven polarization lobes constraining most of the light to the top half of the starshade. In Figure 12 we plot the contrast averaged over a  $\lambda/D$  wide

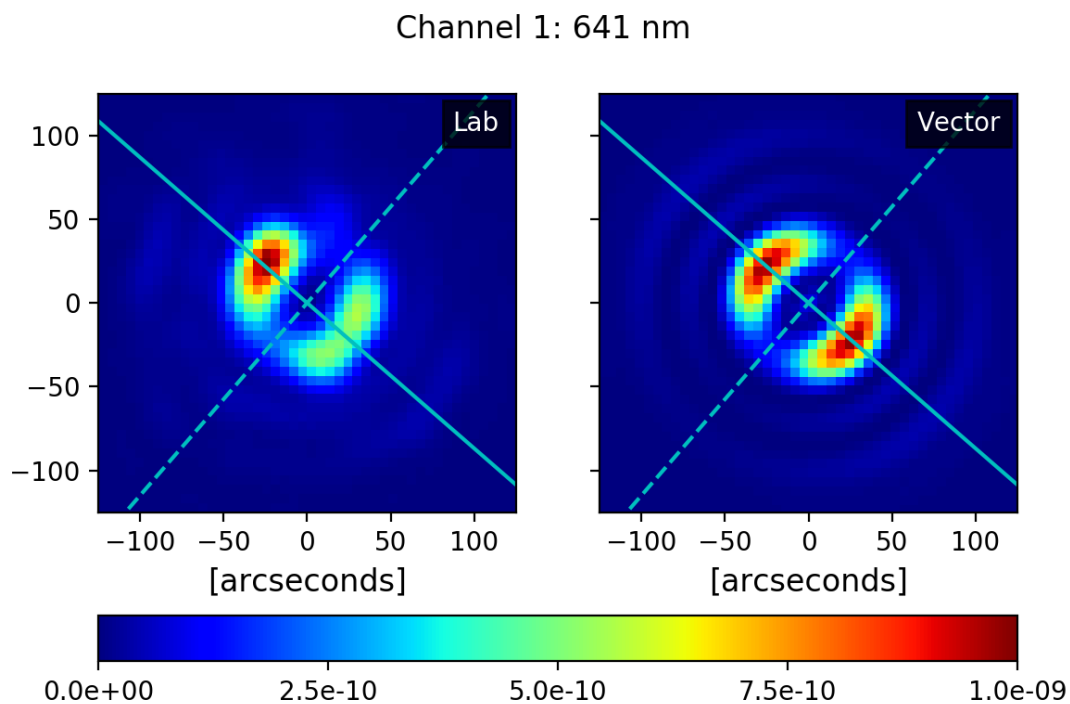


Figure 6: Experimental data (left) and vector diffraction model (right) for Channel 1. Solid and dashed lines are parallel and orthogonal to the polarization direction.

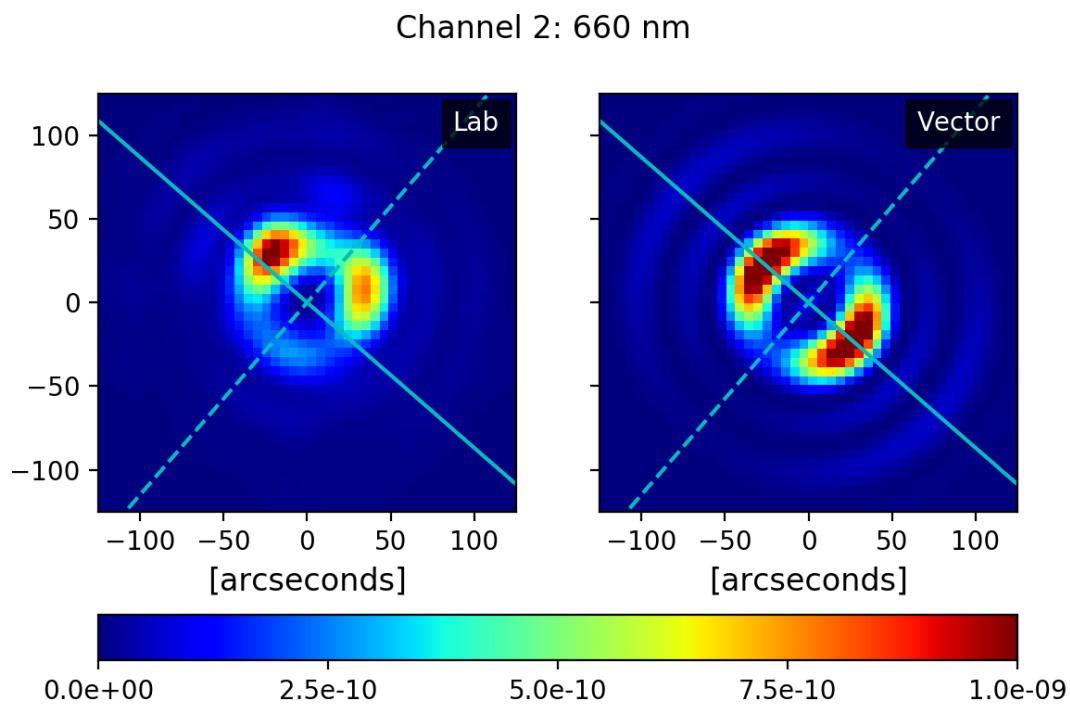


Figure 7: Experimental data (left) and vector diffraction model (right) for Channel 2. Solid and dashed lines are parallel and orthogonal to the polarization direction.

Channel 3: 699 nm

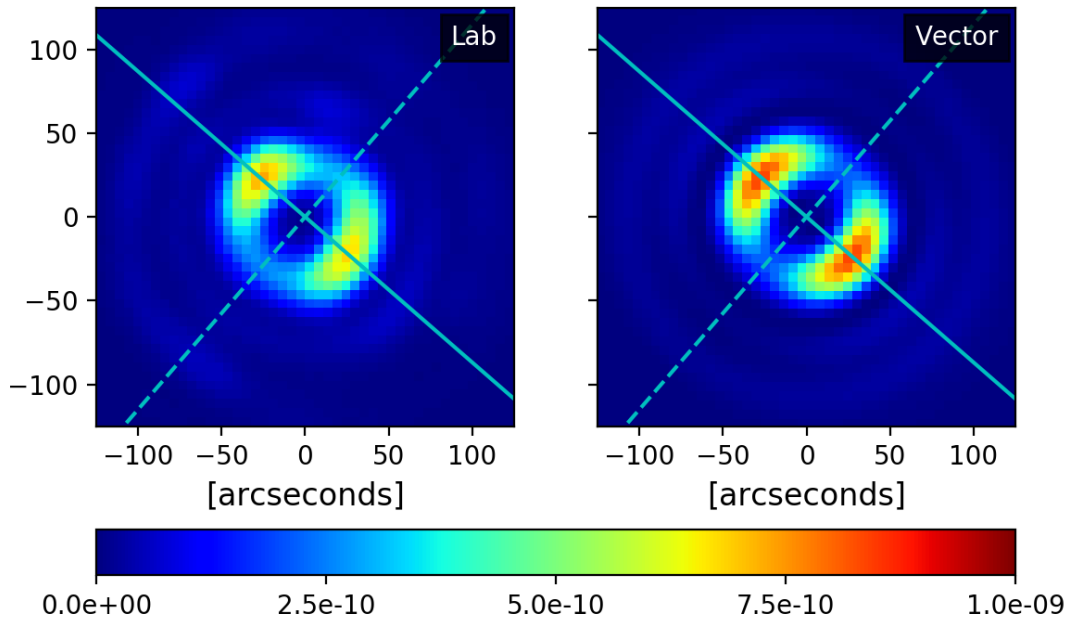


Figure 8: Experimental data (left) and vector diffraction model (right) for Channel 3. Solid and dashed lines are parallel and orthogonal to the polarization direction.

Channel 4: 725 nm

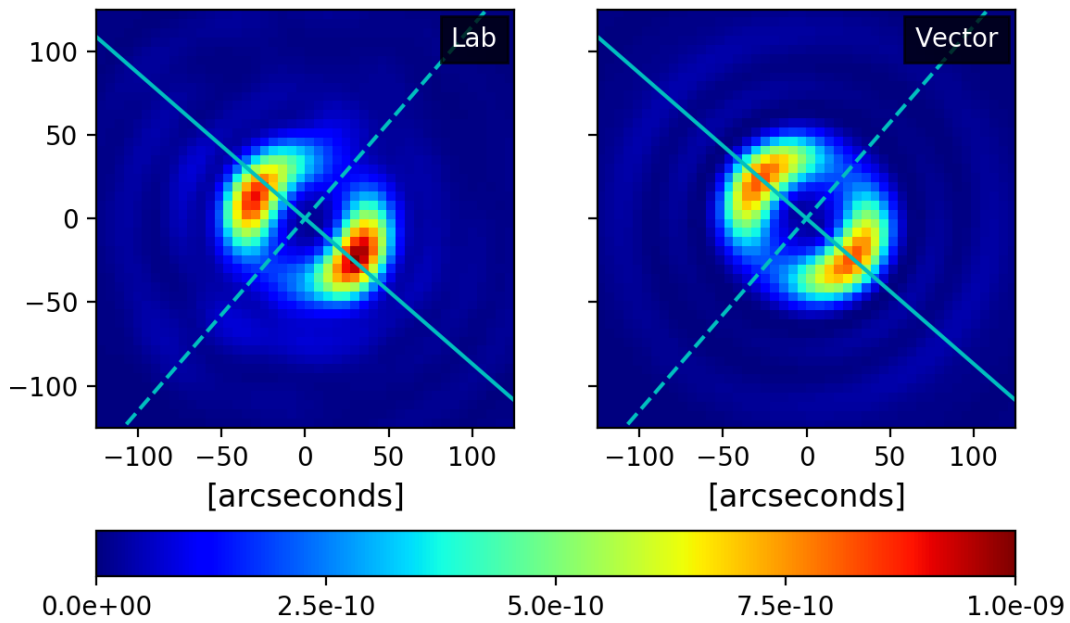


Figure 9: Experimental data (left) and vector diffraction model (right) for Channel 4. Solid and dashed lines are parallel and orthogonal to the polarization direction.

Wavelength Channel	Fraction of IWA with Contrast $< 10^{-10}$	Fraction of $N = 15$ with Contrast $< 10^{-10}$	Fraction of Total Search Space
1	$18 \pm 4 \%$	$71 \pm 10 \%$	$83 \pm 4 \%$
2	$34 \pm 6 \%$	$51 \pm 3 \%$	$77 \pm 3 \%$
3	$2 \pm 2 \%$	$41 \pm 10 \%$	$74 \pm 5 \%$
4	$6 \pm 2 \%$	$31 \pm 7 \%$	$65 \pm 5 \%$

Table 3: The fraction of pixels at the IWA, at the radius where Fresnel number  $N = 15$ , and over the total search area that have a contrast averaged over a  $\lambda/D$  aperture of  $< 10^{-10} - 3\sigma$ . The estimated systematic noise error is  $\sigma = 2.4\%$ .

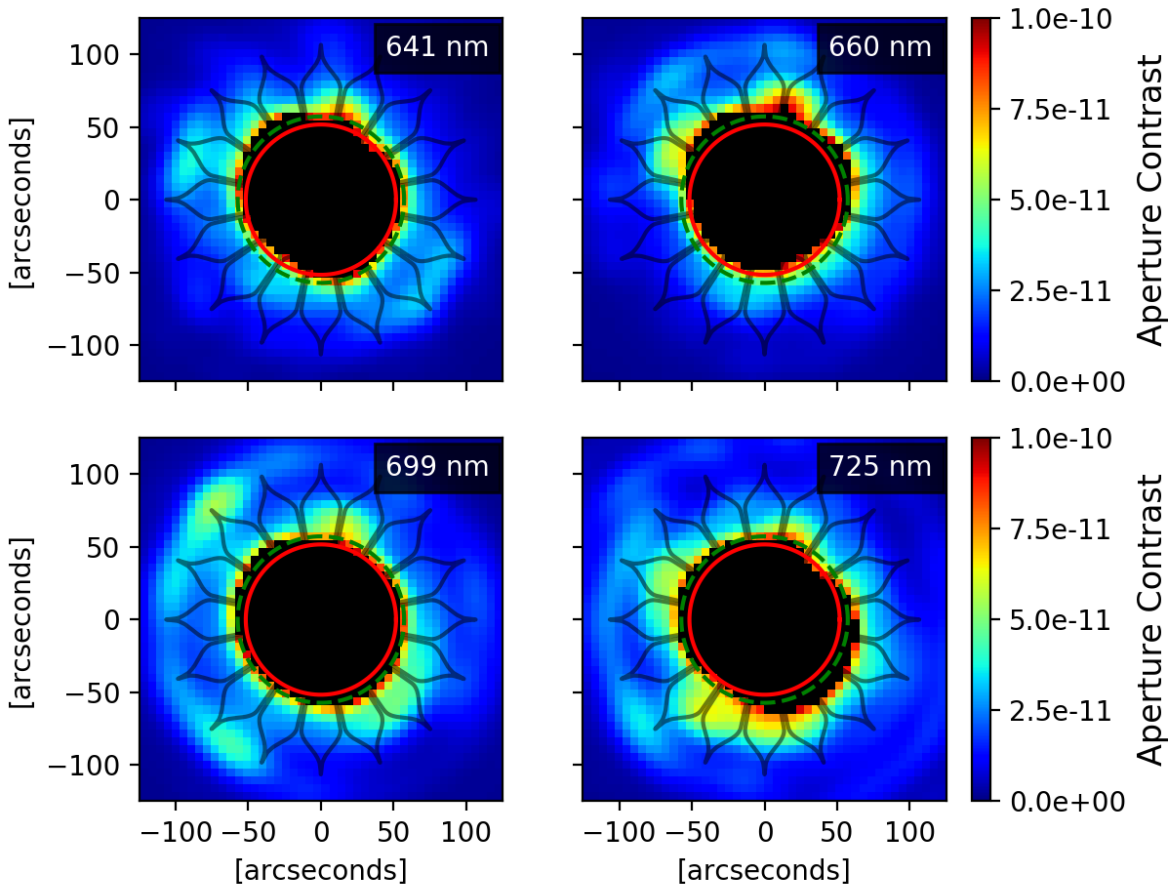


Figure 10: Contrast averaged in  $\lambda/D$  wide photometric aperture centered on each pixel. Black pixels are where the average contrast is greater than  $3\sigma$  below  $10^{-10}$ . Circles are the IWA (red solid) and  $N = 15$  (green dashed).

annulus as a function of radius. The average contrast over the 10% bandpass is  $2.0 \times 10^{-10}$  at the IWA and  $1.3 \times 10^{-10}$  at Fresnel number  $N = 15$ .

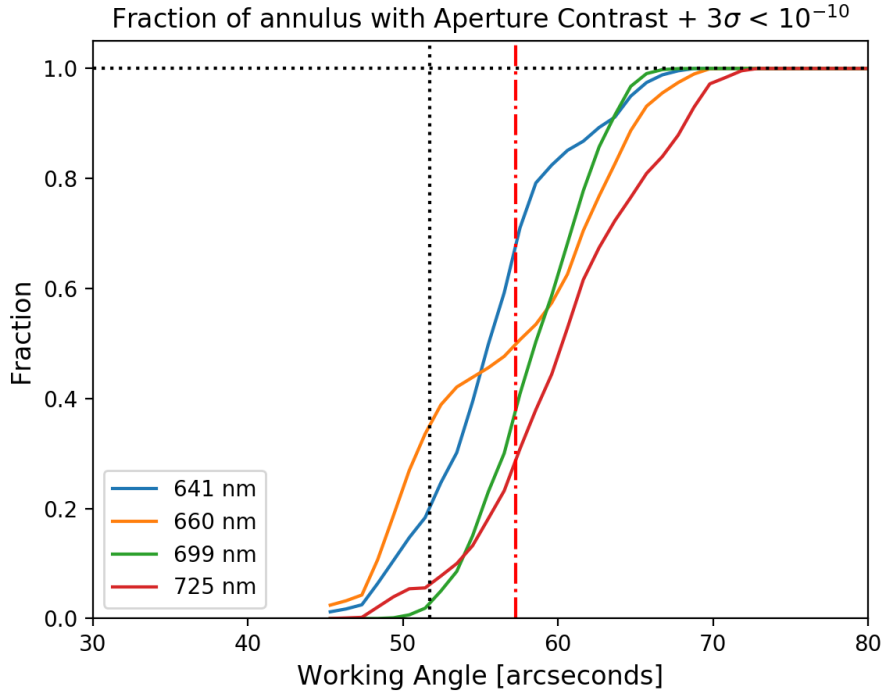


Figure 11: The weighted average fraction of pixels that meet the milestone contrast for all wavelength observations. Vertical lines are the IWA (dotted) and  $N = 15$  (dash-dot).

## 6 Discussion

### 6.1 Comparing M1A and M1B results

Our primary milestone results are presented in Table 3 and Figure 11. These results are consistent with the M1A findings that the milestone is met over a fraction of search space around the IWA, but is limited by the presence of non-scalar diffraction lobes emanating from the narrow gaps between the petals. As we move to longer wavelengths and the PSF of the telescope is broadened, the wings of the lobes place more light at the IWA and the search space that meets the milestone is reduced. This is solely due to the telescope’s lower resolution; working across a wider bandpass did not reduce the starshade’s ability to achieve high contrast (consistent with the starshade’s inherently broadband nature) and the conclusions of M1A still hold.

### 6.2 Model accuracy

The vector models nicely explain the main features observed in the experiment: the position, orientation, and amplitude of the central lobes, and the ringing-down of the diffraction with increasing radius. Still, there remain several unexplained observations. First, the central

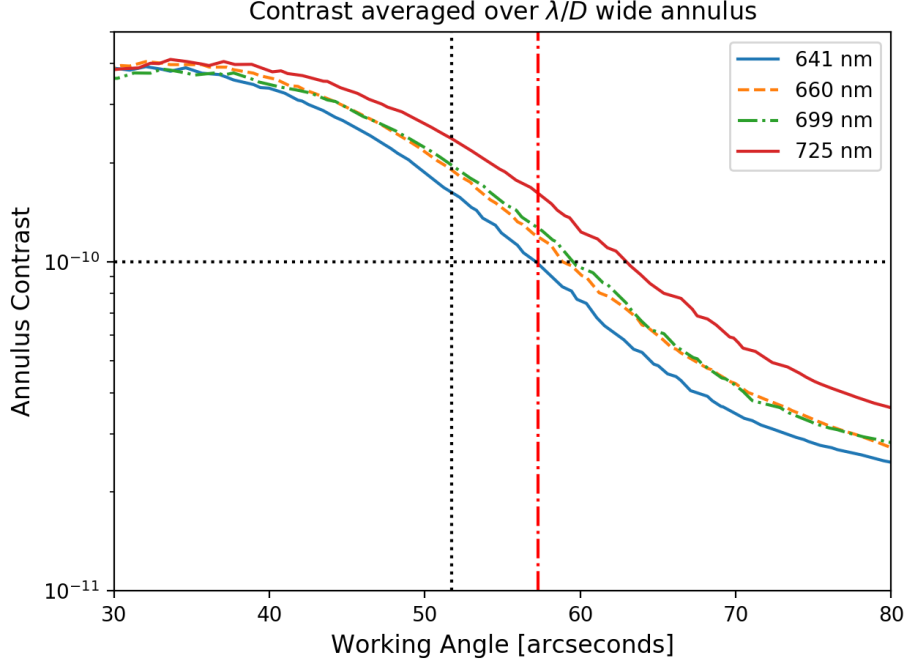


Figure 12: Contrast averaged over a  $\lambda/D$  wide annulus as a function of radial working angle for all wavelength observations. Vertical lines are the IWA (dotted) and  $N = 15$  (dash-dot).

polarization lobes are not quite symmetric, and in one case they are highly distorted. Second, the observed polarization lobes are wider than predicted by the model, especially at the shorter wavelengths. Third, the model predicts some contrast dips that are more prominent than seen in the data (this is best illustrated in Figure 18 in Appendix B). Still, the central lobe effects are largely contained within the IWA, and the contrast dips are not the limiting contrast factors.

### 6.3 Mitigating the thick screen effects

The limiting factor in these experiments is the modification of the electric field due to the interaction of light with the edge of the 2-3 micron thick, gold-coated silicon mask. The effect is largest in the 16 micron wide inner gaps between the petals. There are several possible approaches to mitigating the effect and improving contrast to levels well below  $10^{-10}$  at the IWA. First, we can make the mask thinner as the propagation effect increases with mask thickness. We originally tried to fabricate masks with a top layer of 1 micron thick silicon nitride, but had mixed results due to the fragility of the edge during separation of the open areas from the mask.

A second possibility is to modify the design to account for the thick screen effects. One simple approach is to pull the edges back by 125 nm so that the resulting openings are matched to the scalar design. This would compensate for the amplitude loss but not the phase shift (Figure 4). However, even if this partially compensates the thick screen effects,

the starshade is still dominated by vector propagation and is not testing primarily scalar diffraction.

Third, a larger testbed could be considered. With a larger diameter mask, the thick screen effects play a relatively smaller role. To preserve the Fresnel number and remain in a flight-like diffraction regime, the testbed length grows as the square of the diameter. A 10 cm diameter mask (2x larger than the current one) would require a 308 m long testbed. The minimum enclosure diameter for  $10^{-10}$  contrast is presently not known though preliminary models indicate that it could be as small as 0.5 m.<sup>5</sup> Figure 13 shows the predicted performance of such a larger testbed based on the vector propagation model. At the IWA the contrast is well below  $10^{-10}$  but it is still dominated by the thick screen effects. Rayleigh scattering has the same contrast floor,  $\sim 10^{-11}$ , as long as the Fresnel number is preserved and the illumination cone angle decreases linearly with testbed length (see Appendix A).

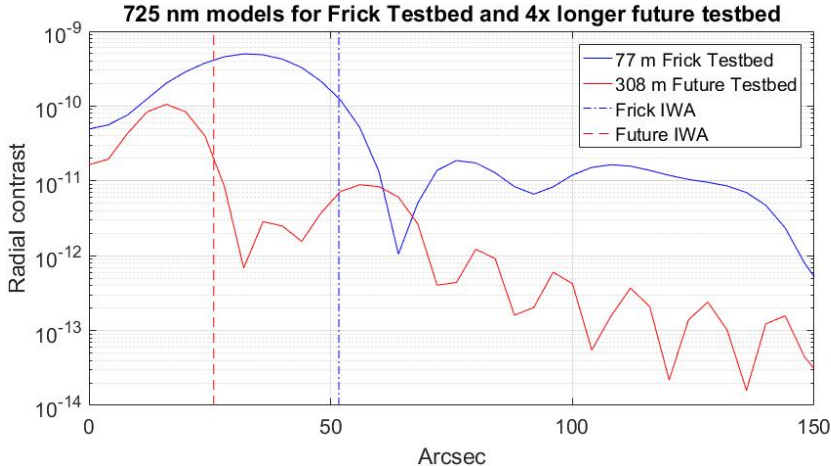


Figure 13: Models showing the expected contrast for the Frick testbed and a 4x longer (308 m) testbed. Models were run with a wavelength of 725 nm under the assumption of a 3  $\mu\text{m}$  thick silicon mask.

## 7 Conclusion

The main conclusion from this work is that starshades show no fundamental barriers to contrast  $< 10^{-10}$  in multiple wavelengths across their designed high-contrast bandpass. Even in still air, and without the aid of active optics, contrast levels of  $10^{-10}$  are observed in proximity of the IWA with a minimum observed contrast of  $2 \times 10^{-11}$  through the open regions of the mask. The performance at the IWA in our experiment is limited by thick screen effects as clearly shown by vector diffraction models, but the full search space is recovered as we move away from the starshade tips. Performance at larger angles is limited by Rayleigh scatter to a contrast level of  $10^{-11}$ .

In spite of the thick screen effects, the laboratory experiments demonstrate contrast levels that would enable a deep and efficient search for exo-Earths in their habitable zones. Additionally, as noted in the M1A report, the desired contrast and IWA can be obtained

by increasing the operational inner working angle beyond the geometric one with a slightly larger, more distant starshade.

The next step for the Frick Testbed is to begin work on Milestone 2, a sensitivity study and model validation experiment to measure the contrast arising from intentionally induced shape errors closely aligned with the errors that comprise the optical performance error budget. These include edge segment displacements, edge segment distortions, single and global petal displacement, and combinations of segment shape and placement errors.

We plan to scale the defects to induce local contrast increases of  $\sim 10^{-9}$  on both the inner and outer starshade. To do so on the inner starshade in the presence of the central polarization lobes, we will orient the mask to place the defect in the valley between the lobes. The outer defect will be isolated from these effects. With a contrast of  $10^{-9}$ , the inner defect will be marginally in the scalar regime; it may be necessary to increase the size of the defect to cleanly separate it from the polarization lobes. We provide examples of measurements in both limits in Appendix B.

## Acknowledgments

This work was performed in part at the Jet Propulsion Laboratory, California Institute of Technology under a contract with the National Aeronautics and Space Administration. Starshade masks were manufactured using the facilities at the Microdevices Lab at JPL. This project made use of the resources from the Princeton Institute for Computational Science and Engineering (PICSciE) and the Office of Information Technology’s High Performance Computing Center and Visualization Laboratory at Princeton University. © 2019. All rights reserved.

## References

- [1] P. Willems, “Starshade to TRL5 (S5) Technology Development Plan,” *Jet Propulsion Laboratory Publications*, 2018. [https://exoplanets.nasa.gov/internal\\_resources/1033](https://exoplanets.nasa.gov/internal_resources/1033).
- [2] A. Harness, S. Shaklan, N. J. Kasdin, K. Balasubramanian, V. White, K. Yee, R. Muller, P. Dumont, S. Vuong, P. Willems, and M. Galvin, “Starshade Technology Development Activity Milestone 1A: Demonstration of High Contrast in Monochromatic Light at a Flight-like Fresnel Number,” *Jet Propulsion Laboratory Publications*, 2019.
- [3] A. F. Oskooi, D. Roundy, M. Ibanescu, P. Bermel, J. Joannopoulos, and S. G. Johnson, “Meep: A flexible free-software package for electromagnetic simulations by the FDTD method,” *Computer Physics Communications*, vol. 181, no. 3, pp. 687 – 702, 2010.
- [4] A. Harness, N. J. Kasdin, S. Shaklan, P. Dumont, and K. Balasubramanian, “Modeling non-scalar diffraction in the Princeton starshade testbed,” in *Proc. SPIE*, vol. 10698, p. 17, 2018.
- [5] A. Harness, S. Shaklan, P. Dumont, Y. Kim, and N. J. Kasdin, “Modeling and performance predictions for the Princeton Starshade Testbed,” in *Proc. SPIE*, vol. 10400, p. 20, 2017.

## Appendix A: Rayleigh Scattering Model

We have extended our analysis of expected light levels in the testbed images due to Rayleigh scattering by air molecules, starting with the same MATLAB model described in the M1A Report. Whereas before we used geometrical optics to model the direct illumination of the camera chamber by the light source through the mask, we now account for the diffraction of the light by the mask when determining the intensity incident upon the air molecules. The diffraction and the molecular scattering cross sections are recalculated for each of the four wavelengths used in the measurements. We have also adapted the model to account for the difference in size between masks DW17 and DW21.

Figure 14 shows the prediction for Rayleigh scattering by atmospheric nitrogen and oxygen alongside the contrast image collected at 641 nm for mask DW21. Comparison to Figure 27 in the M1A Report shows that properly accounting for the diffraction of the source light around the mask features, especially the struts, yields a much closer agreement between the Rayleigh scattering model and the data for regions outside the mask's OWA. Note that the data image has been rotated slightly to make the similarity more evident.

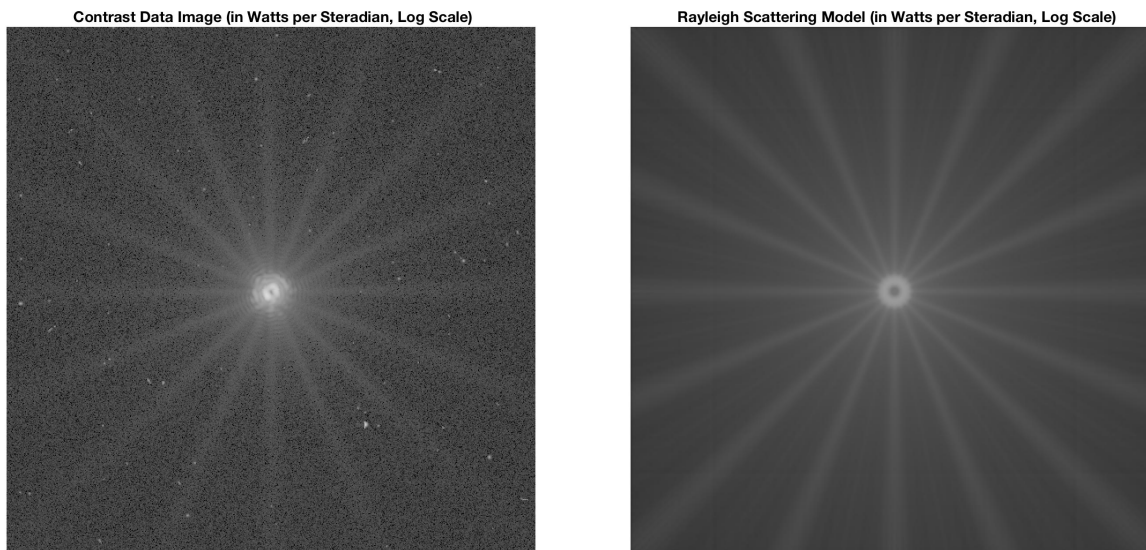


Figure 14: Left: focal plane image of DW21 at 641 nm. The intensity is plotted on a logarithmic scale. Right: Rayleigh model for 641 nm plotted to the same scale.

Figure 15 shows that the Rayleigh model quantitatively accounts for a significant fraction of the contrast light seen just inside of the OWA, and nearly all of the light seen outside the OWA. While the scatter due to atmospheric nitrogen and oxygen are sufficient to account for essentially all of the excess light seen in the spokes for 641 nm and 660 nm, there is still  $\sim 40\%$  of the light in the spokes at 700 nm and 725 nm that they do not account for. A small amount of fine dust suspended in the testbed air only during the long wavelength measurements would explain the observed scattering, but the testbed was sealed during all the measurements reported here. Dust could settle out of the air during the measurement period, but the measurements showing excess scatter were done last.

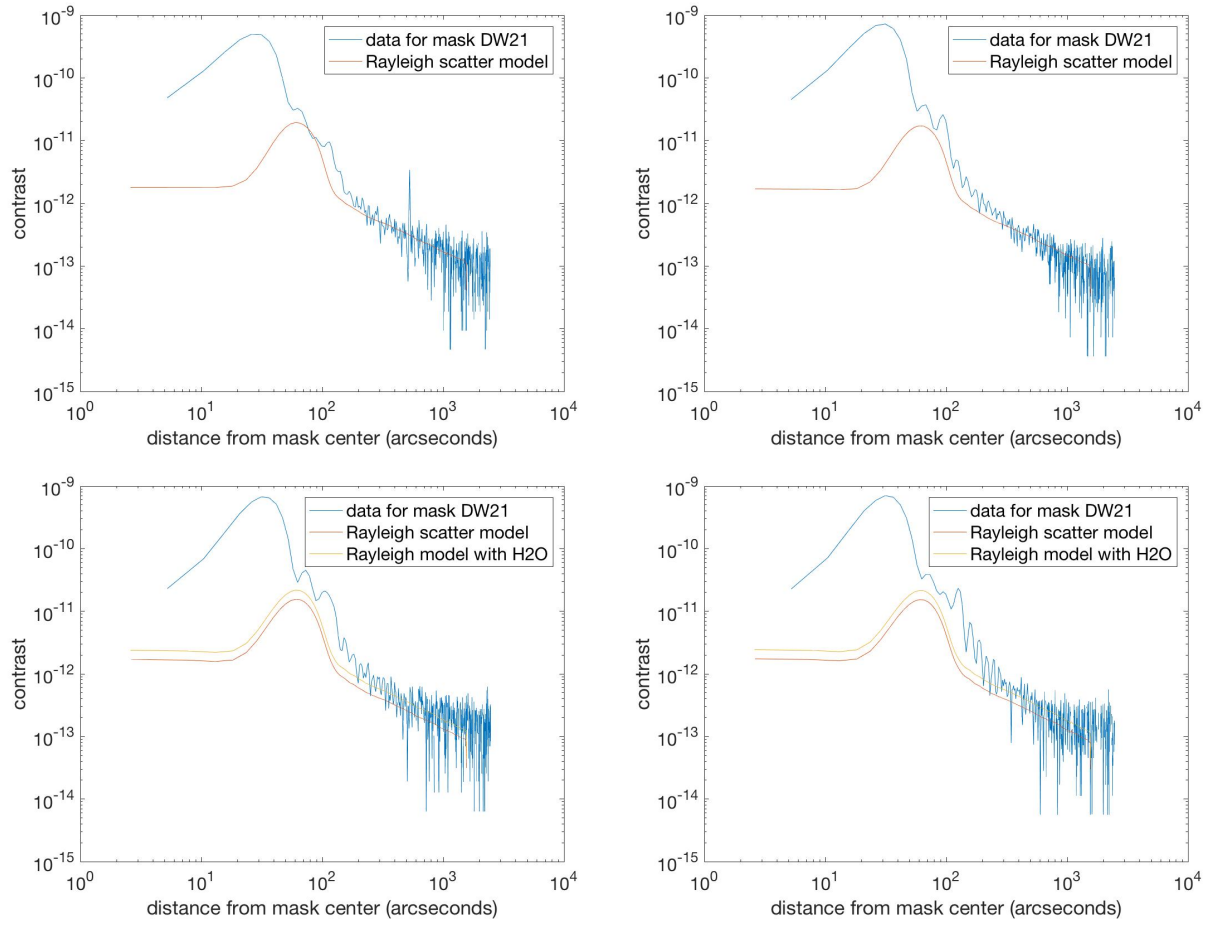


Figure 15: Contrast plotted from the center of the mask outward along a 'spoke' for the data (blue), the dry air Rayleigh scattering model (red), and wet air Rayleigh scattering model for longer wavelengths (yellow). The wavelengths are: upper left, 641 nm; upper right, 660nm; lower left, 700 nm; lower right, 725 nm.

Another possible explanation would be an excess in Rayleigh scattering due to resonant transitions in air molecules near 700 nm and 725 nm. Water vapor in particular shows significant absorption features at those frequencies. Quantifying the expected level of excess scatter from water vapor resonances is beyond the scope of this report, but it is possible to crudely estimate whether it could be as large as is seen in the data. Water vapor typically accounts for 1% of room air, so in order to contribute to the total scattered light at the  $\sim 10\%$  level its scattering cross section must be  $\sim 10$  times that of dry air. The Rayleigh scattering cross section for dry air ranges from  $2.2 \times 10^{-31} \text{ m}^2$  at 641 nm to  $1.4 \times 10^{-31} \text{ m}^2$  at 725 nm. The *absorption* cross section for a water molecule increases from about  $3 \times 10^{-30} \text{ m}^2$  to about  $6 \times 10^{-28} \text{ m}^2$  over this same wavelength region (These figures are averages over the  $\sim 1 \text{ nm}$  bandwidth of the source laser.) The on-resonance *scattering* cross section for a water molecule will generally be less than the on-resonance absorption by a factor of the ratio between the resonance fluorescence decay rate of the molecule’s excited state and the decay rate due to all other mechanisms. Water vapor scattering is consistent with the laboratory data if this ratio is of order 1%. In Figure 15, we show both the ‘dry air’ and ‘wet air’ Rayleigh scattering predictions for the 700 nm and 725 nm data, where the ‘wet air’ model includes enough additional scattering to be consistent with the intensity seen in the spokes well outside the OWA.

The Rayleigh scattering contribution to the contrast in an annulus of one resolution element at the inner working angle is shown in Table 4. Here we used the ‘wet air’ model for 700 nm and 725 nm; even if water vapor is ultimately not the source of the excess scatter, clearly some additional Rayleigh scattering is present.

Wavelength	Contrast at IWA	Suppression
641 nm	$1.6 \times 10^{-11}$	$4.7 \times 10^{-9}$
660 nm	$1.5 \times 10^{-11}$	$4.2 \times 10^{-9}$
700 nm	$1.9 \times 10^{-11}$	$4.7 \times 10^{-9}$
725 nm	$1.8 \times 10^{-11}$	$4.0 \times 10^{-9}$

Table 4: For each wavelength, we present the average contrast contribution at the IWA due to Rayleigh scattering, as well as the contribution to the overall suppression.

Figure 16 shows line plots through the centers of the suppression images, along with the predictions of the suppression floor due to Rayleigh scattering, which is assumed in our model to uniformly illuminate the camera entrance aperture. As is the case for the contrast plots, the Rayleigh model is in good agreement with the observed suppression floor at 641 nm and 660 nm, but about 40% lower for 700 nm and 725 nm unless the ‘wet air’ model is adopted with the same excess scattering used in making the contrast plots in Figure 15.

In the results reported here, Rayleigh scattering sets a noise floor at about 10% of the desired contrast performance of  $10^{-10}$ . It is interesting to ask whether Rayleigh scattering sets a higher noise floor in longer testbeds. The answer is that *the contrast level of Rayleigh scattering at the IWA is independent of the testbed length*, if the testbed and its components are scaled upward in a manner that preserves the Fresnel number and a few other related parameters.

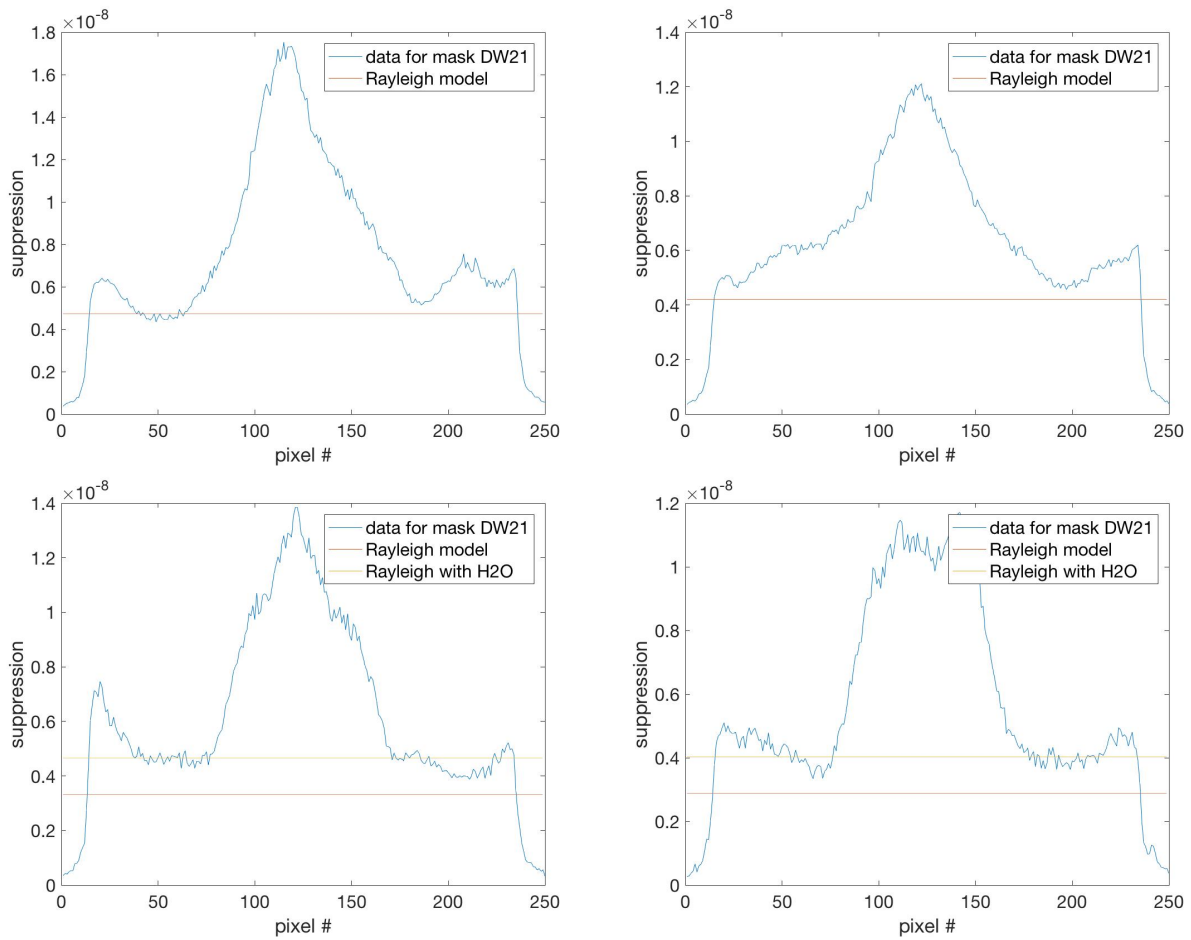


Figure 16: Suppression plotted through the center of the camera pupil for the data (blue), the dry air Rayleigh scattering model (red), and the wet air model (yellow). The wavelengths are: upper left, 641 nm; upper right, 660nm; lower left, 700 nm; lower right, 725 nm.

Namely, if the size of the starshade mask is scaled up by a factor  $n$ , then:

- I the distance from the source to the mask and from the mask to the camera are scaled up by  $n^2$ ;
- II the size of the camera aperture is scaled up by  $n$ ;
- III the plate scale of the camera is scaled down by  $n$ ;
- IV and the divergence angle of the source is scaled down by  $n$ .

The first condition preserves the Fresnel number, the second and third conditions maintain the number of resolution elements across the starshade, and the fourth condition ensures that the light source overfills the mask by the same relative amount.

Although it may be at first surprising, this result is fairly simple to justify. We divide the volume of the testbed into a number of volume elements, and let this number stay the same as the testbed is scaled by the rules above. Now consider how the scattered light from one of these elements varies as  $n$  varies. Given rules I and IV above, which elements are illuminated and which are not is independent of  $n$ . The diameter of the illuminating beam at the mask location grows as  $n$  like the mask, so the intensity there is reduced as  $1/n^2$ ; the intensity at any volume element will be reduced by the same factor. The solid angle subtended by the camera aperture collecting the light from the scatterer will also be reduced by  $1/n^2$ . Together, these reduce the light collected from a single molecule by  $1/n^4$ . However, the volume of the element (and therefore the number of scattering molecules) increases like the testbed volume as  $n^4$ . The net effect is no change with  $n$  in the amount of Rayleigh scattered light collected by the camera. Running the MATLAB model with these scaling relations confirms that the contrast does not change. It therefore does not appear strictly necessary that future starshade optical testbeds need to operate in vacuum, at least as far as Rayleigh scattering is concerned. Should it be desirable that a future testbed not strictly scale from the Princeton testbed in the manner described above, this calculation can be repeated for that specific case.

## Appendix B: Scalar Model Validation using M1A Mask at 725 nm

We have experimentally verified the accuracy of the scalar model at a contrast level of  $10^{-8}$  by measuring the contrast of the M1A mask (DW17) at a wavelength of 725 nm, about 40 nm above its deep suppression cutoff. We compare the DW17 results to M1B (DW21) and show that the M1B results are limited by vector propagation. Recall from Section 2.2 that DW21 is 3.2% larger than DW17 but is otherwise identical in design. DW17 has deep suppression between 600-685 nm, while DW21 is designed to work from 640-730 nm, spanning the 4 laser wavelengths used in the experiment.

The experimental data is compared to the vector and scalar models in Figure 17 (2-D) and Figure 18 (azimuthal average). The upper panels of Figure 17 show that at a peak contrast of  $10^{-8}$ , scalar diffraction is the main contributor, with the thick screen effects, which are

mainly confined to the inner tips, accounting for the innermost ring. The figure also shows that the models do not explain some important localized flux excess and asymmetry. The lower panels shows that with  $10^{-9}$  peak contrast, vector propagation is dominant. The polarization lobes in the vector model are not as high as in the data, but also do not go as deep.

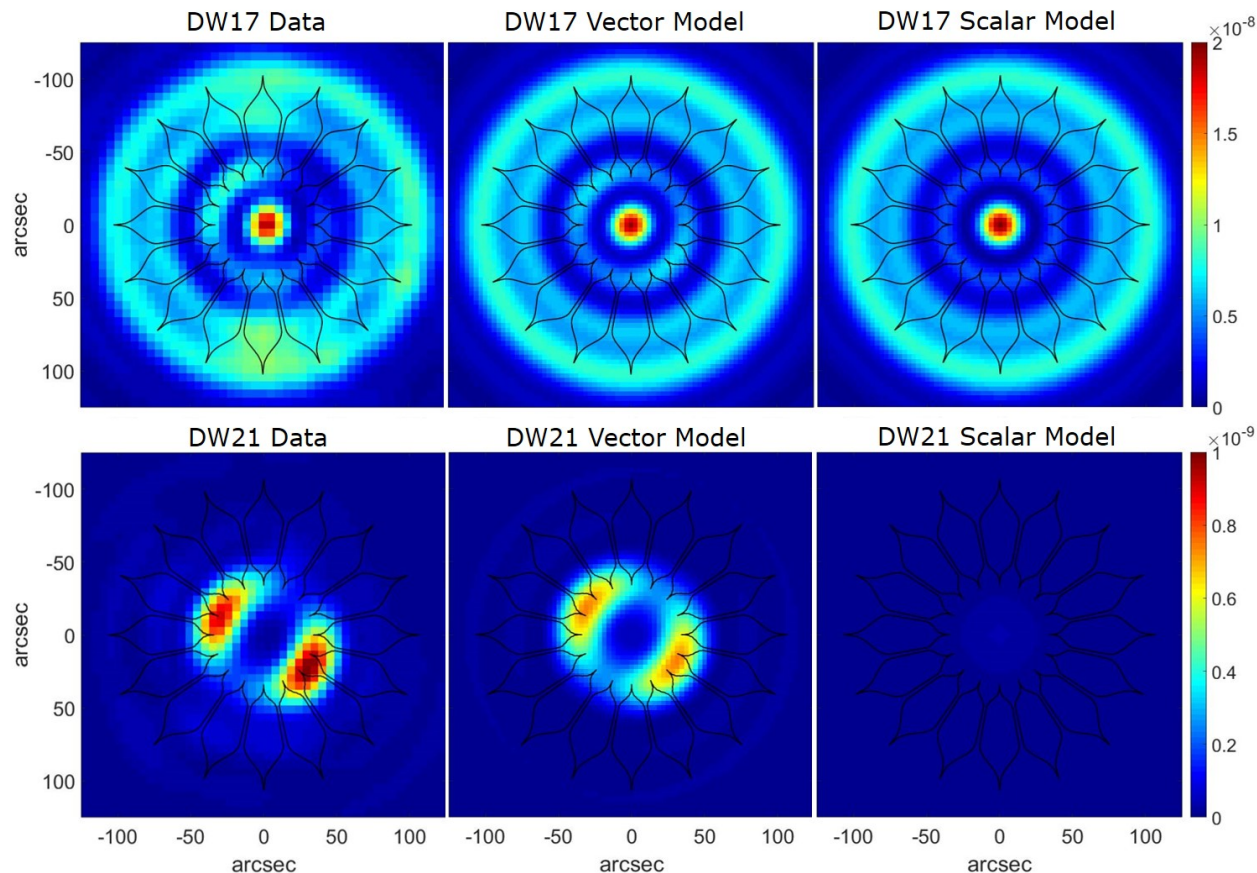


Figure 17: Contrast maps for M1A mask (DW17) and M1B mask (DW21) at 725 nm, and the corresponding vector and scalar propagation models. Note the factor of 20 scale difference between the top and bottom rows.

Meanwhile, Figure 18 shows that propagation models provide an excellent match to the azimuthally averaged data at the higher contrast level of DW17, and are accurate to better than  $4 \times 10^{-11}$  for the deeper contrast with DW21. We have also included the Rayleigh scatter model and added it to the vector model. Rayleigh scatter fills in much of the contrast dips seen in the DW21 diffraction model.

When used outside of the designed high-contrast bandpass, the observed  $10^{-8}$  diffraction pattern matches the scalar model. This gives us confidence that the scalar model will likewise describe the diffraction at deeper contrast levels in configurations where vector propagation is less prominent.

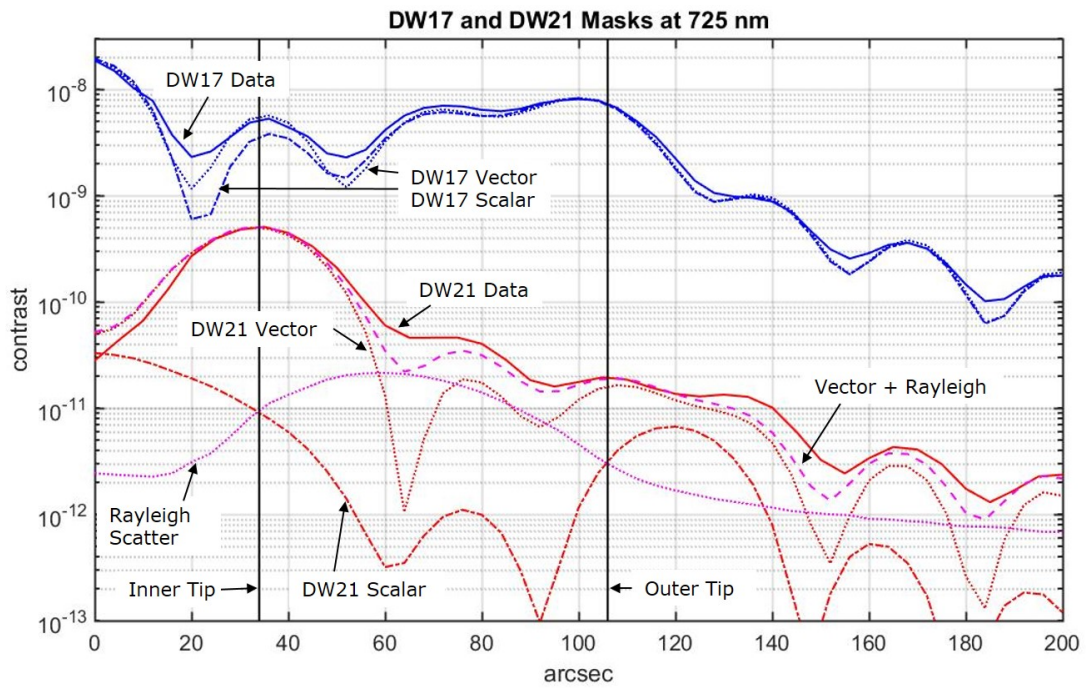


Figure 18: Azimuthally averaged contrast for the M1A mask (DW17) and M1B mask (DW21) at 725 nm, and the corresponding vector and scalar propagation models.